Numerical Calculation and Experimental Validation of Safety Valve Flows at Pressures up to 600 bar

A. Beune and J. G. M. Kuerten

Dept. of Mechanical Engineering, Eindhoven University of Technology, 5600 MB Eindhoven, The Netherlands

J. Schmidt

BASF SE, Safety and Fluid Flow Technology, 67056 Ludwigshafen, Germany

A numerical valve model has been validated to predict the discharge capacity in accordance to the requirements of valve sizing method EN ISO 4126-1 and the opening characteristic of high-pressure safety valves. The valve is modeled with computational fluid dynamics software ANSYS CFX, and the model is extended with the Soave-Redlich–Kwong real-gas equation of state to allow calculations at pressures up to 3600 bar. A unique test facility has been constructed to perform valve function and capacity tests at operating pressures up to 600 bar with water and nitrogen. For gas flows, the numerical results and the experimental data on mass flow rates agree within 3%, whereas deviations in flow force are 12% on average. The inclusion of fluid-structure interaction in the numerical method improves the results for the flow force well and also gives insight into the valve dynamics of an opening safety valve. In a comparison between the experimentally and numerically determined liquid mass flow rates, a model extension accounting for cavitation reduces overpredictions by a factor of 2–20% for smaller disk lifts and decreases the deviations in flow force from 35 to 7%. At higher disk lifts, the effect of cavitation is less, and experimental and numerical mass flow rates agree within 4% and flow forces within 5%. © 2011 American Institute of Chemical Engineers *AIChE J*, 57: 3285–3298, 2011
Keywords: high pressure, safety valve, CFD

Introduction

Worldwide there are numerous industrial applications of high-pressure safety devices as safety valves or rupture disks in the range from 250 to 3600 bar set pressure. Examples are the production of synthesis gas or the polymerization of low-density ethylene at high pressures of typically 1500–3000 bar. Existing standards, such as EN ISO 4126-1,[1] do

not explicitly cover this pressure range, and test facilities are not available for experimental determination of mass flow capacities and opening characteristics. This article presents a numerical tool, which was developed to provide these data. This tool has been validated by experiments at pressures up to 600 bar.

A spring-loaded safety relief valve consists of a compression spring, which presses the valve spindle and disk on the valve seat to seal the pressurized system in case of operating conditions below the valve set pressure. Figure 1 shows the analyzed commercial proportional spring-loaded high-pressure safety valve manufactured by BASF SE with previously
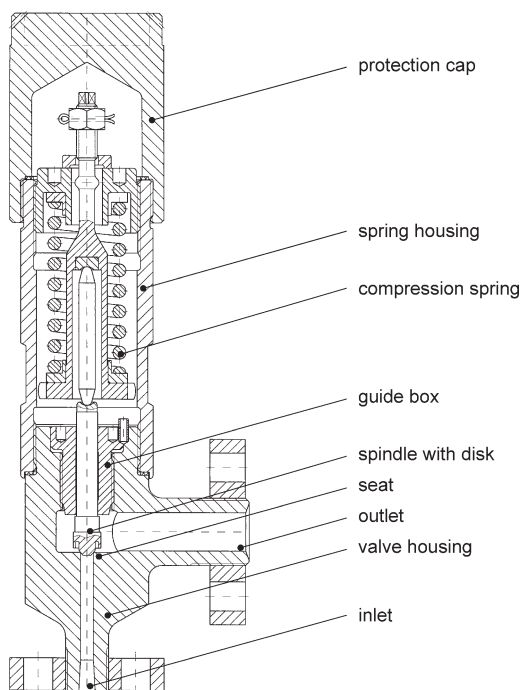

Figure 1. Construction drawing of a high-pressure safety valve.

measured discharge coefficients of 0.266 and 0.308 at the nominal disk lift of 1 mm. During valve opening, a complex flow pattern is formed between the valve seat and spindle with disk. In this region, the geometry forces the flow to be accelerated up to the smallest cross-sectional area and to be deflected. Depending on the thermodynamic state of the fluid, the contour of the flow varies.

Computational fluid dynamics (CFD) is a numerical approach that provides a qualitative and with extra effort also a quantitative prediction of 3-D fluid flows by means of numerical solution of partial differential equations, which describe the flow. Zahariev[2] studied flow behavior in safety valves with the commercial CFD software package CFX TASCflow, where he optimized the valve disk geometry. The validation of the numerical model was limited to force measurements of a single valve experiment series of air with fixed disk lifts at an inlet pressure of only 44 bar blowing off at atmospheric conditions. The predicted and measured flow force and pressure at the disk agree within 5%.

Bredau[3] visualized air flows in simplified pneumatic valve models up to 7 bar in experiments and calculated these with the CFD program TASCflow as well with good agreement. This work also shows the ability of CFD modeling to accurately describe safety valve flows, but this applies only to flows at low pressures. The work of Bürk[4] shows that for higher disk lifts the predicted flow force differs less from the experimental value, although the computed pressure loss in the stagnation area is too small.

The role of CFD in safety valve design in industry is gradually becoming more important. Darby and Molavi[5] calculated viscous correction factors for very viscous fluids through safety valves with the help of CFD. In the work of Föllmer and Schnettler,[6] it is stated that the flow fields agree

with expectations, but quantitative comparisons with experimental data are not given. Furthermore, in recent work of Moncalvo et al.,[7] four mass flow rates of fixed lift safety valve experiments up to 35 bar have been calculated with ANSYS Flo with deviations with respect to the measurements up to 11%.

According to these academic studies, modeling of safety valve flow should be possible with sufficient accuracy, but validation has been considered for low pressures only. In addition, accurate validation data have not been published yet. The capability of a numerical tool for the highly complex safety valve flow can only be assessed when individual flow phenomena that occur in safety valve flows are validated separately.

Challenging flow phenomena occurring in high-pressure safety valve flows are as follows: real-gas effects, choking below the valve disk, flow separation, and condensation. The model parameters of the numerical tool developed in this research have been determined in validation test cases based on reference data from literature ranging from 1-D inviscid flows to 3-D real-gas flows. The cases are chosen such that they display a combination of the relevant physical phenomena. After that gas and liquid flows in a high-pressure safety valve are calculated with the commercial CFD code ANSYS CFX 11.0.

In Section "Standardized Valve Sizing Method" of this article first the quantities used in the valve sizing standard are explained. Then in Section "Numerical Model," the numerical tool and its modeling parameters are introduced. In Section "Experimental Methodology," the high-pressure test facility and the data acquisition method to acquire the validation data are presented. In Section "Results for Liquid Valve Flow" and "Results for Gas Valve Flow," numerical results for steady valve flow are compared with experiment and analyzed for both liquid water and gaseous nitrogen flows. Section "Conclusions" consists of concluding remarks about the validity of the current valve sizing methods as well as the opening characteristics at high pressures. More detailed information can be found in Ref. 8.

Standardized Valve Sizing Method

The flow capacity calculation of a safety valve according to EN ISO 4126-1[1] is based on isentropic flow through a nozzle with a correction factor for flow losses and redirection of the flow, the so-called discharge coefficient K_d. For incompressible nozzle flow, the mass flow rate calculation is based on the Bernoulli equation with a correction for viscous flow effects, whereas for compressible flow the equation of state (EoS) for a perfect gas is used. The discharge coefficient K_d is the correction factor between the mass flow rate of an isentropic flow in a nozzle $\dot{m}_{nozzle}$ and the experimentally determined mass flow rate in a safety valve $\dot{m}_{exp}$

$$K_d = \dot{m}_{exp}/\dot{m}_{nozzle}. \tag{1}$$

This discharge coefficient should only account for flow losses and redirection of the flow caused by the valve geometry. Therefore, the dimensionless flow coefficient C calculated with the nozzle model should only cover the thermodynamic state changes

$$\dot{m}_{\text{nozzle}} = CA_0\sqrt{2p_0\rho_0} \qquad (2)$$

where p_0 is the stagnation inlet pressure and ρ_0 is the stagnation inlet density. In case of a safety valve flow, the nozzle throat A_0 is represented by the valve seat area. The dimensionless flow coefficient for nonflashing liquids $C = C_l$ is

$$C_l = K_v\sqrt{1 - \eta} \qquad (3)$$

where K_v is a viscosity correction factor and η is the ratio of the backpressure p_b at the outlet of the valve and the inlet stagnation pressure p_0

$$\eta = p_b/p_0 \qquad (4)$$

For noncondensing and nonreacting vapors and gases, the dimensionless flow coefficient $C = C_{\text{g,id}}$ is derived from the perfect-gas EoS at stagnation conditions[9,10]

$$C_{\text{g,id}} = \sqrt{\frac{\kappa_0}{\kappa_0 - 1}\eta^{\frac{2}{\kappa_0}}\left[1 - \eta^{\frac{\kappa_0 - 1}{\kappa_0}}\right]} \qquad (5)$$

For a calorically perfect gas, the adiabatic or isentropic exponent κ_0 is defined as the ratio between the specific heats

$$\kappa_0 = \frac{c_{\text{p,0}}}{c_{\text{p,0}} - R_s} \qquad (6)$$

where $R_s = R/M$ is the specific gas constant, R the molar gas constant, M the molar mass, and $c_{\text{p,0}}$ is the specific heat at ideal gas conditions.

When the backpressure at the outlet of the valve p_b equals the pressure at the (truncated) nozzle throat, a further reduction of the backpressure has no effect on the mass flow rate. Then, the flow is choked at the nozzle throat and the critical pressure ratio is fixed. In case of a calorically perfect gas, the critical pressure ratio η_{crit} equals[10]

$$\eta_{\text{crit}} = \left(\frac{2}{\kappa_0 + 1}\right)^{\frac{\kappa_0}{\kappa_0 - 1}} \qquad (7)$$

Equations 5 and 7 are equivalent to the equations given in the standard EN ISO 4126-1[1] for determination of the discharge capacity for any gas under critical flow conditions

$$q_m = 0.2883C\sqrt{\frac{p_0}{v_0}} \qquad (8)$$

$$C = 3.948\sqrt{\kappa_0\left(\frac{2}{\kappa_0 + 1}\right)^{(\kappa_0 + 1)/(\kappa_0 - 1)}} \qquad (9)$$

with q_m the theoretical specific discharge capacity in kg/(h mm^2), the pressure p_0 in bar (abs.), and the specific volume at actual relieving pressure and temperature v_0 in m^3/kg.

It is noted that at high pressures (or low temperatures) the gas cannot be considered to behave as a perfect gas anymore, so that the stagnation properties deviate from the calorically perfect gas approximation and have to be calculated using a real-gas EoS. Then, the density is corrected with a compressibility factor Z, and the adiabatic exponent κ has to be calculated with a real-gas EoS as well. The effect of real-gas effects on the discharge coefficient and the flow force on the disk will be discussed in section "Results for Gas Valve Flow".

Numerical Model

To describe the 3-D flow phenomena in a safety valve by means of CFD, first the mathematical models to generate thermodynamic property data in a consistent way, such as the real-gas EoS, are introduced. Second, the discretization method by means of a numerical grid is presented followed by the solution method of the numerical model.

Mathematical models

The conservation laws of mass, momentum, and energy are numerically solved in the commercial software package ANSYS CFX.[11] To model the effects of turbulence, the shear stress transport model[12] has been chosen, because of the available two-equation Reynolds-averaged Navier–Stokes models in CFX, this model gives the highest accuracy with acceptable calculation times and numerical stability. The good performance of this turbulence model has been verified with benchmark simulations, such as a 1-D shock tube, a 2-D supersonic ramp, and axisymmetric (real gas) nozzle flows and 2-D and 3-D (simplified) valve models, that represent relevant physical effects occurring in high-pressure safety valves.

The conservation equations have to be completed with definitions of the fluid properties in the form of an EoS. At high pressures (or low temperatures), the gas cannot be considered to behave as a perfect gas anymore, so that the stagnation properties deviate from the calorically perfect gas approximation and have to be calculated from a real-gas EoS.

To calculate real-gas flows at pressures up to 3600 bar with the CFD code, the temperature has to range from 100 to 6000 K and the pressure from 0.01 to 10000 bar for numerical stability during the iterative solution process. Therefore, look-up tables with the thermodynamic properties: specific heat at constant pressure c_p, specific volume v, specific heat at constant volume c_v, pressure-specific volume derivative at constant temperature $\left(\frac{\partial p}{\partial v}\right)_T$, speed of sound a, specific enthalpy h, specific entropy s, dynamic viscosity μ, and thermal conductivity λ have to be generated. These quantities are functions of temperature linearly divided into 400 points and pressure logarithmically divided into 400 points.

The cubic Redlich–Kwong (RK) EoS relates the pressure to the temperature and specific volume of a supercritical gas. This equation was extended by Soave[13] for improved accuracy for larger and polar molecules. For many gases, the coefficients of this EoS are tabulated, and with the help of mixing rules it can also be applied to gas mixtures, which is beneficial for practical applicability of the valve sizing models and the numerical tool.

The calculation of the compressibility factor Z and specific heat capacity at constant pressure c_p with the SRK EoS has been compared with IUPAC (2008)[14] with the specific heat at constant reference pressure c_p of 0.01 bar with an

uncertainty of 0.3–0.8% as input. For reduced temperatures $T_r > 1.5$, the accuracy of both variables is within 5% at pressures up to 3600 bar. This is the highest valve inlet pressure to be calculated with the numerical method. Closer to the critical point where the gradients of the variables are large the deviation is up to 10%. The equations to calculate the thermodynamic property tables are given in the Appendix.

Discretization

For the complex valve geometry, an unstructured hexahedral grid is used that is the best compromise between geometrical flexibility and the possibility to refine the mesh locally without deteriorating the mesh quality. In the regions with the largest flow gradients, the geometrical mesh quality, quantified by grid-line orthogonality and expansion rate of the element volumes, has to be sufficiently high to limit truncation errors and increase the robustness of the solver. The inlet and outlet are modeled as openings at specified values of the stagnation inlet pressure and temperature and static pressure and temperature at the outlet both at subsonic conditions. The walls of the high-speed flow are considered adiabatic. The commercial high-pressure safety valve actually starts at the small pipe after the reducer. The inlet of the computational domain at the reducing transition piece is further enlarged to obtain a sufficiently low Mach number of $Ma = 0.01$. The pressure loss in the inlet pipe is always far below 3%, so that the pressure loss rule, which is required for stable valve operation, is not violated. The outlet of the computational domain is equal to the outlet of the valve.

The computational domain is discretized with 1.1 million hexahedral grid cells with the mesh generator FLUENT GAMBIT 2.4.6 (Figure 2). For the axisymmetric section of the safety valve, first a planar mesh is created with size functions only and a density increase ratio as low as 1.025. The densest regions of the planar mesh are near the seat and the lifting aid, where the nodal wall distance is 0.05 mm. The height of the structured boundary layer cells is 0.01 mm with a forced edge-length ratio of unity at the last mesh cell to achieve a gradual increase to the unstructured cells in the bulk flow region. The smallest radius of this 2-D mesh is 1 mm from the inlet symmetry axis to be able to revolve the mesh around this axis at an angle of 180°. As a result, 80 mesh cells in azimuthal direction are obtained without generating reduced mesh cells at the symmetry axis. In this way, the mesh is regular in the azimuthal direction with the advantage of locally increased densities and high mesh quality of the planar axisymmetrical mesh. After revolving the planar mesh, the remaining half cylinder volume around the inlet symmetry axis becomes a structured mesh extruded from a planar unstructured mesh at the top surface of the truncated spindle cone.

For the side outlet, an unstructured planar mesh is generated with the same mesh density as the revolved 3-D mesh that is extruded to the outlet. This means that at the surface between the revolved mesh and the side outlet the face meshes have different topologies, so that only a general grid interface can connect both meshes within the computational domain. The drawback is that interpolation inaccuracies
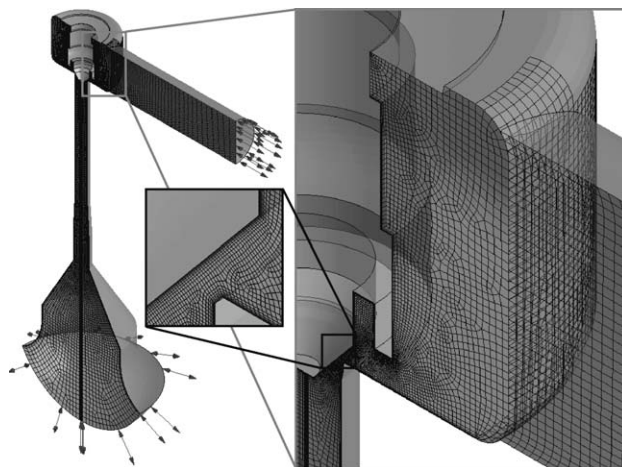

Figure 2. Computational domain of a steady safety valve flow simulation.

occur, but this interface is located in a region where no large gradients occur.

Solution method

In the CFD software package ANSYS CFX, the numerical discretization is node based and it uses shape functions to evaluate the derivatives for the pressure gradient term and the diffusion terms in the momentum, continuity, and turbulence quantities equations. The Navier–Stokes equations are discretized in a collocated way and solved by an algebraic multigrid solver. To avoid pressure–velocity decoupling, a robust interpolation scheme similar to Rhie–Chow interpolation[15] is used. CFX solves the conservation equations of mass and momentum in one fully coupled system of equations.[11] The turbulence equations are pairwise solved as well, and the energy equation is solved separately.

CFX uses advection schemes such as first-order upwind differences and numerical advection with a specified blend factor. This blend factor can be varied between 0 and 1 to vary between a first- and second-order differencing scheme and control numerical diffusion. The high-resolution scheme option will be chosen, which maintains the blend factor as closely to 1 as possible without violating the boundedness principle that could result in nonphysical oscillations in the solution. For the turbulence equations, the first-order accurate scheme is sufficient. In unsteady simulations, a second-order accurate linear multistep method is applied for the time integration of the mass, momentum, and energy equation, whereas a first-order backward Euler scheme is applied for the turbulence equations.

Experimental Methodology

For validation of the numerical method, an experimental test facility has been constructed for determining the discharge capacity and opening characteristics of high-pressure safety valves for water and nitrogen at operating pressures up to 600 bar. In this section, first the construction of this test facility is summarized. Second, the especially designed and calibrated measurement equipment for measurement of
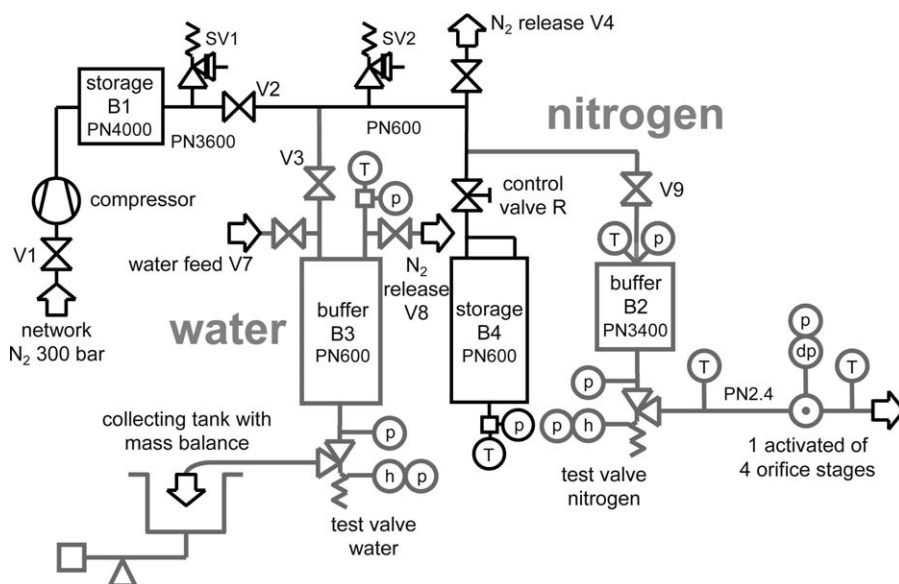
Figure 3. High-pressure valve test facility with partially used parts in gray for valve tests with either water or nitrogen.

local values of pressure and temperature, valve disk lift, and the integrated quantities mass flow rate and force on the valve disk is presented. Finally, it is demonstrated how the data are collected in a valve test example with nitrogen.

High-pressure test facility

In the test facility, the major valve characteristics, such as opening pressure, overpressure, blowdown, lift, and operating stability, described in the standard EN ISO 4126-1[1] are measured. Valve tests are conducted at well-defined measurement conditions for various fluids, valve types, valve sizes and springs, and at various operating pressures.

The test rig consists of four vessels (Figure 3). Vessel B1 is connected to the compressor, which provides a pressure up to 4000 bar. Either buffer vessel B3 is in use for valve tests with water or buffer vessel B2 for valve tests with nitrogen. Prior to a valve test the storage vessel is pressurized with compressed nitrogen at a higher pressure than the operating pressure of the test valve. During a valve test, high-pressure nitrogen in the storage vessel B4 expands into buffer vessel B3 filled with water or buffer vessel B2 filled with nitrogen and pushes the test fluid in the buffer vessel through the test valve located at the opposite side of the feed lines of one of the buffer vessels. A valve R is used to

control the pressure rise followed by a period of constant pressure during blow-off of the test valve, while the pressure in the storage vessel decreases.

Measurement techniques

In contrast to most existing test facilities, the disk lift is measured with a displacement sensor inside the pressurized valve spring housing with protection cap (Figure 4, left). Elevated pressures will build up in the spring housing during measurement, which leads to an additional pressure force on top of the valve disk. Therefore, an analog magnetostrictive noncontacting linear displacement sensor in combination with a guiding extension is used, with minimum added friction, minimum added mass of the moving components, and minimum added volume of the housing. This sensor can cope with severe valve vibrations with an inaccuracy of <0.01 mm.

The flow force F_{flow} acting upon the valve disk is derived from the deflection of the compression spring that is prestressed to a certain set pressure p_{set} of the valve. At this set pressure, the valve should start to open and the spring force equals the set pressure times the seat area A_0. At nonzero disk lifts h, the spring is deflected further to generate a higher spring force depending on its spring stiffness k_{spring}
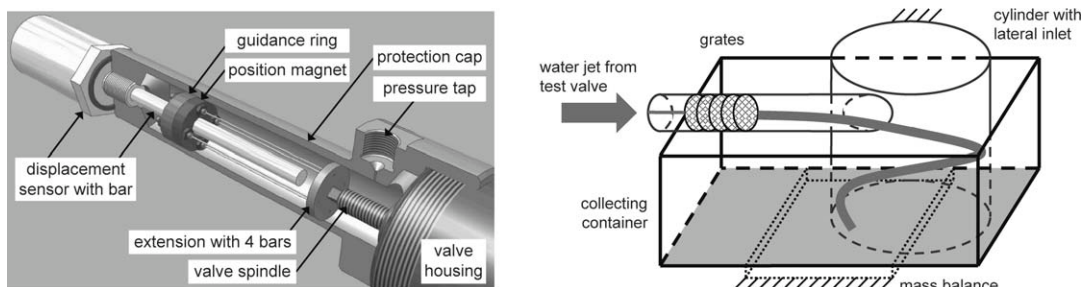

Figure 4. Disk lift measurement setup and liquid mass flow rate measurement setup.

$$m\ddot{h} = F_{\text{flow}} + p_{\text{set}}A_0 + k_{\text{spring}}h + F_{\text{friction}} \qquad (10)$$

For steady flow, the momentum force generated by the moving components with equivalent mass m becomes zero. Because of the free movement of the valve spindle the friction force is considered negligible as well. The flow force can also be measured with an additional force sensor that acts as a mechanical stop at variable maximum disk lift and still allows accurate force measurement when the spindle moves to this stop.

The liquid mass flow rate is measured with a mass balance at the low-pressure side after the safety valve where the water is collected in a tank. A similar way of measuring mass flow rates using a force sensor is given by Koenig and Friedel.[16] In this way, the measurement method does not disturb the flow upstream. The capacity of this tank is 1.6 m^3 for a flow of 40 kg/s during 40 s. Before the liquid flows into the collecting tank, it first passes five grids vertically located in a horizontal cylinder (Figure 4, right). These grids decelerate the jet flow from the safety valve, so that the stream divides and decelerates further in the vertical cylinder. In this way, the momentum of the flow will minimally disturb the reading of the mass balance. This mass flow rate measurement system enables measurement of constant mass flow rates with an uncertainty between 2 and 3.5% for time windows of 4 s.

Gas mass flow rates are measured at the atmospheric pressure side after the test valve by means of subcritical orifices in accordance to standard EN ISO 5167.[17] To cover the measurement range of 0.02–10 kg/s, four orifice stages are used with an inaccuracy less than 1%.

The pressures are measured with gauge pressure sensors with inaccuracies of ∼0.1% after calibration. Temperatures in the vessels are measured by thermocouples type K with an absolute accuracy of 1 K and the temperatures in the gas metering equipment with shielded PT100 resistance thermometers with 0.3 K.

Data acquisition

Multiple series of valve relief tests are carried out in which the safety valve to be tested remains mounted in the test facility. In these tests, all points of stationary valve operation are collected, from which the opening characteristic is deduced. After each valve test series, the geometry of the valve seat and valve spindle is measured on a 3-D-coordinate machine with an inaccuracy of 0.9 μm. It is noted that all investigated safety valves are based on the same construction drawings of which Figure 1 is deduced from the assembly drawing. Any small geometric difference caused by mechanical wear up to a few tens of a millimeter is taken into account in both experimental and numerical analysis.

Figure 5 shows the distribution of all measured quantities of a safety valve experiment with gaseous nitrogen. At $t = 16$ s the safety valve opens at 300 bar measured just before the test valve p_{valve} and the same value in the buffer vessel p_{buffer}. The maximum disk lift of this proportionally opening high-pressure safety valve is reached around $t = 30$ s and remains constant during 4 s at $h = 1.61$ mm. At this time, the pressure in the valve spring housing increases up to $p_{\text{housing}} = 30.1$ bar.
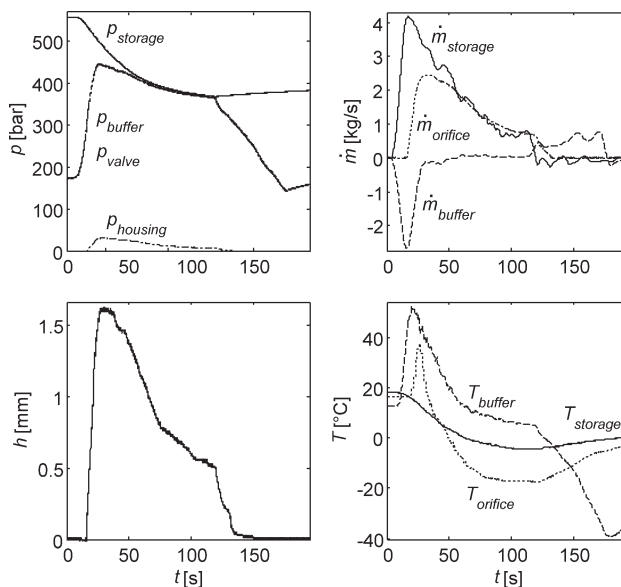

Figure 5. Example of valve test with nitrogen.

The temperature in the storage vessel T_{storage} continually decreases until the test valve closes again. Furthermore, because of a fast pressure rise in the buffer vessel, its temperature T_{buffer} increases from 13 to 52°C and drops immediately after opening of the safety valve. The same temperature variations are observed for the orifice T_{orifice}, which are on an average 20° lower because of the flow expansion in the safety valve.

At almost steady, state conditions, i.e., small variations of pressure, disk lift, and mass flow rates, sample ranges of the measurements have been selected. Then, the disk with compression spring deflected to a certain lift is in force equilibrium with the flow force. In other words, the disk floats on the passing flow without any restrictions. Typical averaging times are between 1 and 100 s.

Results for Liquid Valve Flow

First, the results of the numerical model are compared with experimental data for liquid flow. Then, the influence of cavitation on the valve model performance is presented and discussed.

Comparison

For validation of the numerical method, four averaged stationary measurement points from test series at a set pressure of 50 bar and two at a set pressure of 375 bar are chosen. Figure 6 shows the experimental and numerical results as a function of the dimensionless disk lift h normalized to the valve seat diameter $d_0 = 8$ mm. At disk lifts below the standardized minimum equal to the valve-specific nominal disk lift of 1 mm, the mass flow rate is overpredicted by 41% for tests at $p_{\text{set}} = 375$ bar and by 21% for 50 bar set pressure. The forces are underpredicted with deviations up to 30% for the test series at $p_{\text{set}} = 375$ bar and up to 35% for the test series with 50 bar set pressure. At the highest disk lifts of each test series, satisfactory agreement is found.
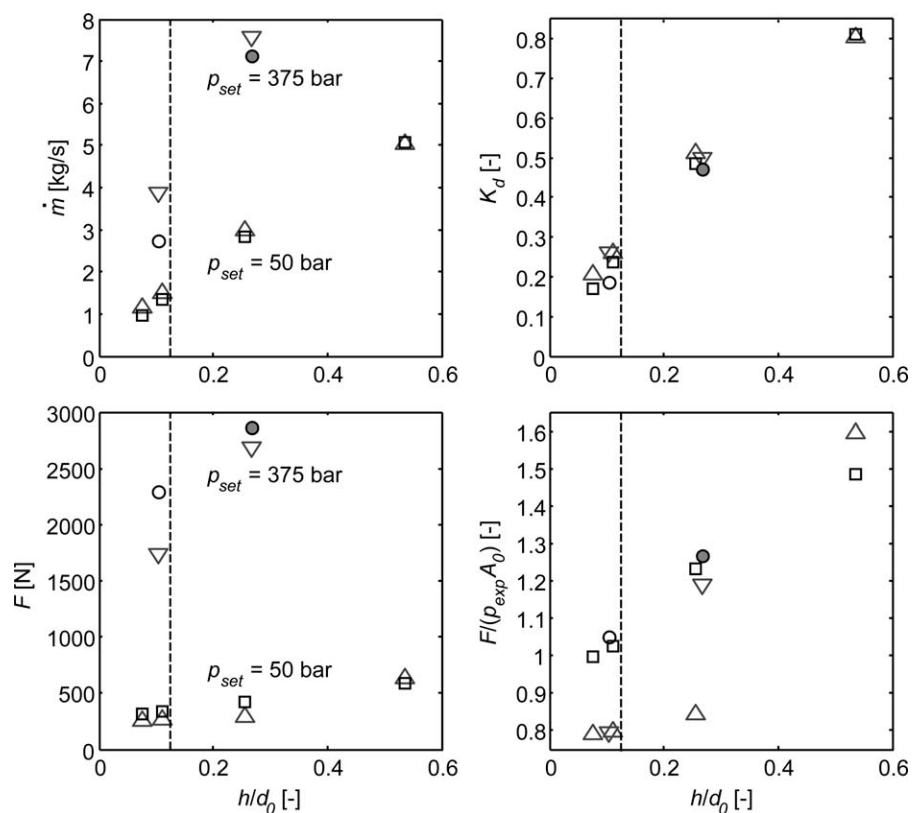
Figure 6. Comparison of experimental and computed mass flow rates and disk forces for water of safety valve test series at set pressures of 50 and 375 bar and temperatures between 283 and 293 K.

□: exp. p_{set} = 50 bar; ○: exp. p_{set} = 375 bar; △: CFX p_{set} = 50 bar; ▽: CFX p_{set} = 375 bar; dashed line = nominal disk lift of 1 mm. The gray-filled circles represent the measurement with mechanical stop with additional force sensor.

Inclusion of cavitation model

Possible reasons for the differences between the experimental and numerical results are the occurrence of cavitation and degasification of nitrogen dissolved in water. Both potential error sources are not included in the numerical model. Although especially at high pressures the amount of dissolved nitrogen can be high, increased dissolution of nitrogen is a less probable reason because of the short exposure of the liquid to high pressures during a valve test. On the other hand, cavitation already occurs at absolute pressures in the order of 10 mbar for water as both experimentally and numerically shown in valves by Beinert.[18] Especially in recirculation areas and diverging ducts cavitation can significantly reduce the effective flow cross-sectional area. To investigate the effect of cavitation on mass flow rate and flow force, a simple cavitation model has been added to the numerical valve model. This model is not intended to explain the observed discrepancies between experiment and numerical simulation quantitatively, but only serves to show that cavitation is an important reason for the discrepancies.

This cavitation model is based on the Rayleigh–Plesset equation, which models the mass transfer between the liquid and the vapor phase by describing the growth and collapse of a vapor bubble in liquid. The rate of vaporization and condensation is controlled by liquid–vapor pressure differences derived from a mechanical balance. This model does not take any thermal effects into account. The total interface mass transfer rate per unit volume $\dot{m}_{lg}$ for vaporization is modeled as[19]

$$\dot{m}_{lg} = F \frac{3 r_g \rho_g}{R_B} \sqrt{\frac{2}{3} \frac{|p_v - p|}{\rho_l}} \operatorname{sign}(p_v - p) \qquad (11)$$

where F is an empirical factor equal to 50 for vaporization, r_g the volume fraction of the gas phase, and $R_B = 1 \times 10^{-6}$ m is the radius of the nucleation sites.[11]

When the local pressure is higher than the vapor pressure, any vapor present in the fluid will condense at a relatively slow rate. In that case, the variable r_g in Eq. 11 needs to be replaced by $r_{nuc}(1 - r_g)$, F is equal to 0.01, and $r_{nuc} = 5 \times 10^{-4}$ is the empirically determined volume fraction of the nucleation sites. This initial volume fraction necessary for numerical stability is still three orders of magnitude less than the computed volume fraction where cavitation actually occurs. At the inlet and outlet boundaries, the volume fraction is set to zero.

The cavitation model is implemented as a homogeneous multiphase model with assumed no-slip velocity conditions between the two phases. The cavitation appears as a volume source term in the continuity equation that is solved in a separate transport equation. The vapor phase is modeled as a gas with constant material properties at 25°C with a corresponding vapor pressure of 31.69 mbar.
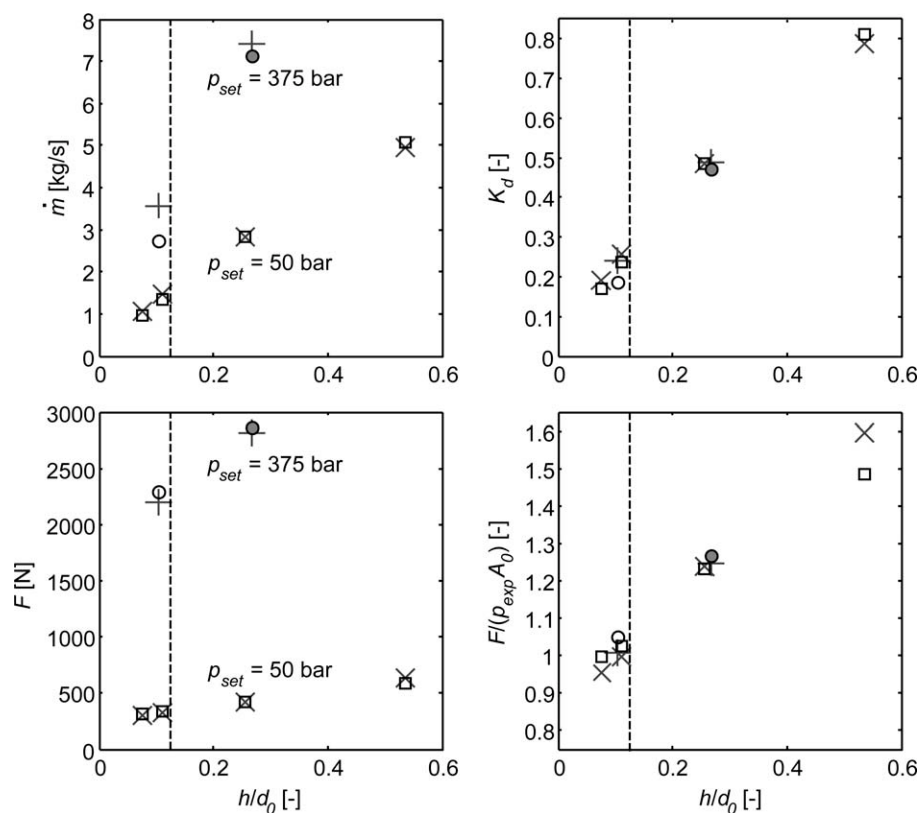
Figure 7. Comparison of experimental and computed mass flow rates and disk forces with water of safety valve test series at set pressures of 50 and 375 bar and temperatures between 283 and 293 K with cavitation model.

□ exp. p_{set} = 50 bar; ○: exp. p_{set} = 375 bar; ×: CFX p_{set} = 50 bar; +: CFX p_{set} = 375 bar; dashed line: nominal disk lift of 1 mm. The gray-filled circles represent the measurement with mechanical stop with additional force sensor.

Figure 7 shows the results of the simulations extended with the cavitation model shown as plus and cross symbols compared with to the experimentally determined mass flow rates and disk forces. The simulations with cavitation lead to a significantly better agreement with experiment. Deviations in the mass flow rate are gradually reduced by a factor of 2–23%, whereas deviations in the flow force are strongly reduced from 35 to 7% at lower disk lifts. At the highest disk lifts, the mass flow rates deviate down to 4 and 3%, respectively, and the flow forces 5 and 0.5%, respectively, when the cavitation model is included.

Table 1 shows the numerical values of the measured and computed discharge coefficients. The geometrical discharge coefficient $K_{d,geom}$ is defined as the ratio between the minimum flow cross-sectional area A_{min} and the seat area A_0. It can be seen that the measured discharge coefficient is always significant lower than the geometric discharge coefficient even when the geometric discharge coefficient is unity. The reason is that for incompressible flow the pressure loss occurs in the whole valve geometry.

Figure 8 shows contour plots of the solution variables pressure p and liquid volume fraction r_1 at the symmetry plane of the valve housing. At the lowest disk lift $h/d_0 = 0.076$ the numerical results show the occurrence of cavitation in the geometrically smallest cross section of the flow. In this area, the pressure is higher than in the simulations without cavitation and the water vapor volume fraction is close to zero at the lower part of the seat. This limits the effective flow area and hence the mass flow rate. At the highest disk lift $h/d_0 = 0.54$, the flow remains single phase between the valve seat and spindle, because cavitation starts after passing the spindle. As a result, the pressure under the spindle is not directly affected.

In conclusion, it is possible to use this numerical method for basically incompressible liquid flows at high pressures, where compressibility mainly stems from cavitation effects and hardly from the weak compressibility of the liquid itself. However, it is not known to what extent dissolution of nitrogen gas into the liquid affects the flow. Therefore, it is recommended to extend the cavitation model for high pressures

Table 1. Numerical Values of Data Points of Safety Valve Test Series with Water with Cavitation Model Included

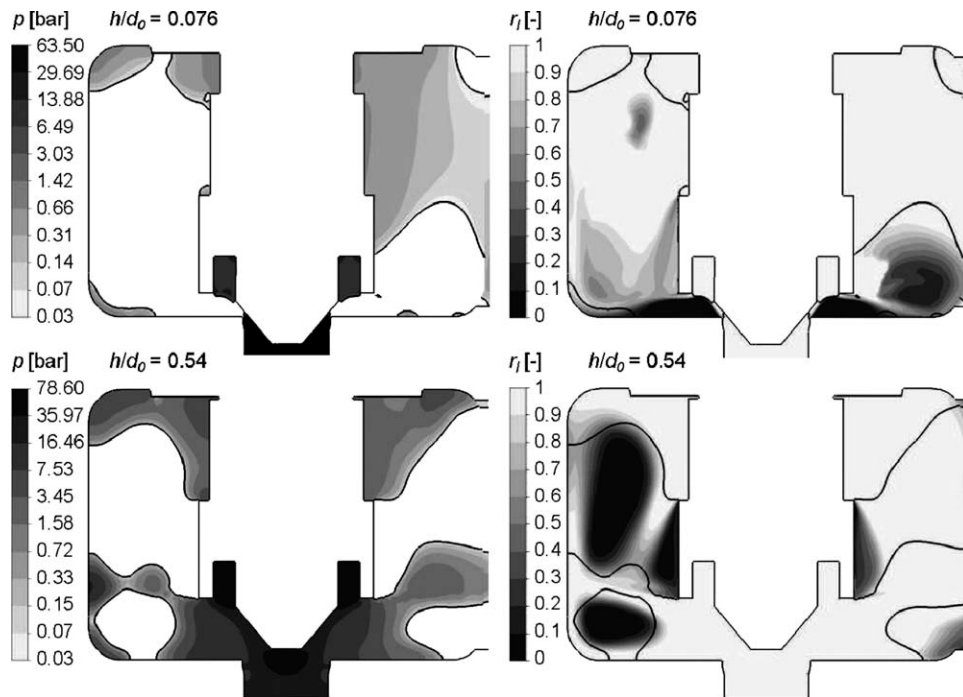| p_{set} (barg)	50	50	50	50	375	375
p_0 (bar)	63.5	65.8	68.3	78.6	434.1	449.7
h/d_0	0.076	0.111	0.255	0.536	0.104	0.268
$K_{d,geom} = A_{min}/A_0$	0.202	0.291	0.622	1	0.276	0.654
$K_{d,exp}$	0.170	0.236	0.485	0.812	0.186	0.474
$K_{d,CFX+cav.}$	0.189	0.257	0.486	0.789	0.239	0.488

Figure 8. Left: Contour plots of logarithmically scaled pressure at symmetry plane of safety valves at p_{inlet} = 63.5 bar at h/d_0 = 0.076 and p_{inlet} = 78.6 bar, h/d_0 = 0.54 both at T_{inlet} = 293 K. Right: Contour plots of the same valve flow with the liquid volume fraction r_l.

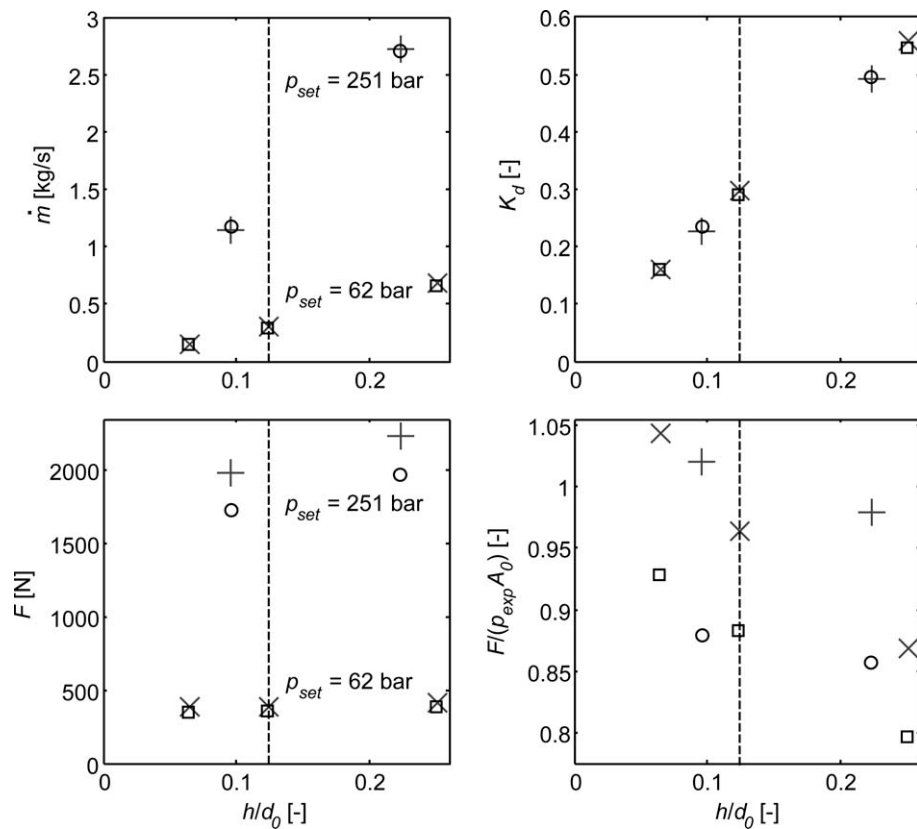The white lines represent the saturation pressure line.

Figure 9. Comparison of experimental and computed mass flow rates and disk forces with nitrogen of safety valve test series at set pressures of 62 and 251 bar and temperatures between 274 and 306 K.

□: exp. p_{set} = 62 bar; ○: exp. p_{set} = 251 bar; ×: CFX p_{set} = 62 bar; +: CFX p_{set} = 251 bar; dashed line: nominal disk lift of 1 mm.

Table 2. Numerical Values of Data Points of Safety Valve Test Series with Nitrogen

p_{set} (barg)	62	62	62	251	251
p_0 (bar)	73.3	79.9	95.1	387.2	453.8
h/d_0	0.065	0.124	0.252	0.096	0.223
$K_{d,geom} = A_{min}/A_0$	0.194	0.329	0.626	0.257	0.564
$K_{d,exp}$	0.161	0.290	0.547	0.236	0.498
$K_{d,CFX}$	0.160	0.298	0.558	0.227	0.493

to account for heat transfer and compressibility effects of the vapor phase. Also, the empirical evaporation and condensation rates that delay or accelerate the growth and collapse of cavitation bubbles may have to be adjusted. Furthermore, the rate of dissolution at high pressures has to be quantified.

From the comparison between the results at the lower set pressure of 50 bar and the higher set pressure of 375 bar, it can be deduced that in the investigated high-pressure region neither the discharge coefficient nor the normalized disk force depends on the set pressure of the safety valve. In other words, a liquid valve flow is scalable to higher pressures even when cavitation or dissolution has a significant effect on the flow.

Results for Gas Valve Flow

In this section, first the results of the numerical model are compared with experimental data for gas flow. Next, the flow dynamics of a safety valve is discussed to explain discrepancies in the results.

Comparison

Figure 9 shows the results of the numerical simulations of low-pressure and two high-pressure averaged measurement points of the gas experiments. The mass flow rates of all points show deviations with experimental data below 3.6%. Consequently, the discharge coefficient calculated as described in the standardized valve sizing method according to EN ISO 4126-1[1] with real-gas property data turn out to be independent of the operating pressure in the range from 73 to 453 bar consistent with the experimental results. In contrast, the disk forces show a deviation between 8 and 11% for the three low-pressure measurement points and around 14% for the two high-pressure points.

Table 2 presents the numerical values of the measured and computed discharge coefficients. For compressible valve flow, the measured discharge coefficient is at the smallest disk lifts and high pressure two times closer to the geometric discharge coefficient than at the lowest pressure. This is probably due to real-gas effects of the flow.

Figure 10 shows the Mach number, pressure and temperature distribution of the left part of the symmetry plane of the same safety valve. In the left plot, high Mach numbers are present in the supersonic flow area with repetitive plumes, where the last plume is detached from the other ones. This shape is similar to overexpanded nozzle flows, where various reflected waves form a diamond pattern throughout the free jet flow. The limited space in the housing prevents the flow from further expansion, so that a second large expansion area with a strong shock at the outlet is necessary to increase the entropy to balance with the thermodynamic state with lower potential energy at the outlet.

For visibility reasons, the pressure contours in the middle of Figure 10 are plotted on a logarithmic scale with an increased minimum value of 10 bar instead of the computed minimum absolute pressure of 74 mbar at the secondary large supersonic area in the outlet. Because of the elevated pressure in the valve housing, the minimum pressure in the supersonic flow area equals 8 bar. The flow expands from the inlet pressure of 452.8 bar to a pressure of 75 bar in the cavity of the lifting aid and to 150–210 bar on the tip.

In the valve tests also the pressure of the spring housing is measured. At the measurement points, this pressure is constant as well, so that dynamic effects and pressure losses that would occur in the small gap connecting the valve housing with the spring housing do not have to be taken into account. As a result, only the connecting face between the
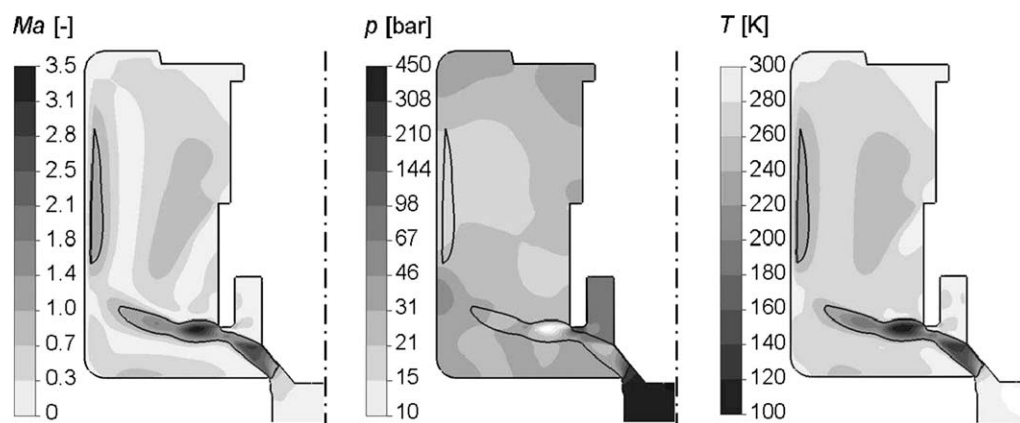

Figure 10. Contour plots of Mach number, pressure, and temperature of left part of symmetry plane of simulation for nitrogen, $p_{inlet} = 452.8$ bar and $T_{inlet} = 306$ K at $h/d_0 = 0.22$.

The black line in all three figures represents the sonic flow line at which $Ma = 1$. The pressure contour plot is logarithmic.

Table 3. Sensitivity Analysis of Ideal Gas vs. Real Gas Flow of Nitrogen in the Test Valve with Disk Lift 1.0 mm and Inlet Temperature 175 K

p_0 (bar)	3.2	16	79.9	400	2000
Z_{id}	1	1	1	1	1
κ_{id}	1.4	1.4	1.4	1.4	1.4
$K_{d,id}$	0.304	0.305	0.305	0.305	0.305
$F_{id}/(p_0A_0)$	0.63	0.98	0.96	0.96	0.97
Z_{SRK}	0.99	0.94	0.77	1.28	4.45
κ_{SRK}	1.41	1.44	2.01	5.19	9.84
$K_{d,SRK}$	0.302	0.303	0.292	0.295	0.286
$F_{SRK}/(p_0A_0)$	0.62	0.92	1.02	1.04	1.09
dK_d (%)	0.95	0.72	4.40	3.32	6.94
$d\dot{m}$ (%)	0.22	−3.1	−18.5	−18.9	38.8
dF (%)	1.6	6.1	−5.6	−7.4	−11.4

gap with a tolerance of 0.1 mm and the valve housing is defined as a separate wall boundary condition. This measured pressure is in this valve test at the highest operating pressure of 452.8 bar equal to 34 bar. The numerically obtained pressure is 27 bar.

In the right of Figure 10, the minimum temperature limit of real-gas property tables of 100 K is only reached in supersonic flow areas with Mach numbers higher than 3.4. An additional simulation with a homogeneous binary mixture to allow equilibrium vapor–liquid phase changes resulted in a reduction to 62 K with a maximum liquid mass fraction of 0.15. Nevertheless, this effect reduces the disk force by only 3% when the condensation would occur at thermodynamic equilibrium.

The effect of nonideality of the real-gas EoS has been assessed by means of safety valve flow simulations for nitrogen with a perfect gas EoS at a disk lift of 1.0 mm. The stagnation temperature of $T_0 = 175$ K at the valve inlet is chosen as close as possible to the critical point of nitrogen where the nonideality is the largest to achieve a constant reduced temperature of $T_r = 1.39$. The stagnation pressure p_0 is varied from 0.094 to 58.9. The results are summarized in Table 3.

It can be seen that in the ideal gas approximation a 4.45 times too large density and seven times too high isentropic exponent κ_{id} lead to mass flow rate differences up to 39% compared with the real-gas approximation. Nevertheless, the difference in discharge coefficient remains below 7%, because the ideal gas flow is scalable when the material properties are constant. The nonlinearity of the real gas flow with compressibility factor varying from 0.72 to 6.94 becomes more evident in the dimensionless flow force where 3-D effects play a larger role. The real-gas approximation shows an increasing flow force compared with the constant ideal gas flow force with a difference up to 11%. Note that the comparison is only made at nominal disk lift. The opening pressure of a safety valve depends on the flow force development just when the valve opens. A more detailed study of the nonideal flow effects on an opening safety valve can be found in Ref. 8.

Dynamic gas valve flow

In the comparison between the numerical and experimental results of gas valve, flow deviations in the flow force around 12% were observed. A numerical analysis did not show significant sensitivities of the flow force to changes in the computational domain, the mesh density, and the turbulence model, nor when transient flow effects or condensation effects were taken into account. The experiments showed that the opening characteristic is strongly affected by mechanical wear of the contact surfaces of the valve sealing. Consequently, the opening pressure changes after repeated valve testing. As a result, the indirect measurement of the flow force with the spring deflection and the operating pressure when the valve actually starts to open is assumed to be too inaccurate.

To gain more insight in the flow force development when the valve starts to open, the dynamic opening of a safety valve is simulated by the inclusion of fluid-structure interaction (FSI) in the numerical method. In this way, the flow force when the valve is closed can be directly compared with the small force changes when the valve is open. The acceleration $\ddot{h}$ of the spindle with disk during valve movement is given by Newton's law

$$\ddot{h} = \frac{F_{flow} - k_{spring}(h + h_0) - m_{spindle}g}{m_{spindle}} \quad (12)$$

where $m_{spindle}$ is the equivalent mass of the moving parts of the valve and g is the gravitational constant.

A series of simulations with inclusion of this law and with multiple moving meshes are necessary, because the mesh deformations are large and the valve geometry is complex. For numerical stability, it is necessary to have connected calculation domains even when the valve is closed. Therefore, the starting grid of a closed valve corresponds to the smallest experimentally detectable disk lift of 0.01 mm. Each numerical grid is predefined with a factor of 1.5 larger disk lift compared with the previous one and starting from a disk lift of 0.01 mm. This results in a total number of 17 predefined meshes.

In this way, the mesh quality parameters orthogonality, expansion, and aspect ratio are preserved as much as possible during opening and closing of the valve. Also, discretization errors that occur in the transfer of the solution variables between two grids with different topology are minimized by gradually varying the time step such that the simulation stops within 1 nm disk lift of the next predefined mesh.

Figure 11 shows the results of transient simulations with multiple meshes of the axisymmetrically modeled safety valve with nitrogen. The simulation starts on the predefined mesh with disk lift $h = 0.01$ mm, initial spring force based on set pressure $p_{set} = 400$ bar and spring stiffness $k_{spring} = 253,280$ N/m, a constant 10% overpressure at the inlet $p_{exp} = 440$ bar, outlet pressure 1 bar, equivalent mass of the moving components $m_{disk} = 0.7662$ kg, and simulation time step size $dt = 2 \times 10^{-6}$ s.

The dashed lines represent the results of quasi-steady simulations, which are converted to the time domain by solving Newton's law with values of the disk force interpolated between the steady-state solutions starting at $t = 0$ s, initial velocity $\dot{h} = 0$ m/s, and initial spring displacement h_0 that is exactly the same as used in the transient (solid lines) simulation with multiple meshes. It can be seen that the force continually decreases up to 15% at 2-mm disk lift. This
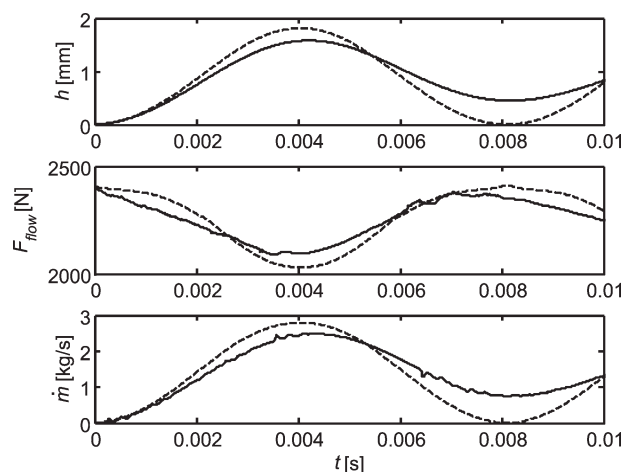
Figure 11. Disk lift, flow force, and mass flow rate vs. time of an FSI simulation with nitrogen gas.

Solid: dynamic; dashed: quasi-steady.

behavior is in agreement with experiments. Because the disk lift has been measured with a frequency of 100 Hz, not enough measurement data are available for comparison of this spring-mass system with experimental data.

Moreover, it can be seen that the static simulation does not have any damping. A damping term in the equation of motion (12) would have the form $\beta \dot{h}$ with $\beta > 0$ on the left-hand side. From a physical point of view, the damping accounts for flow-history effects and the velocity of the valve, which is equal to zero in the calculation of the flow force in the quasi-steady simulation. The results of both simulation show that the difference between the flow force in the two approaches, ΔF is correlated with the velocity of the disk $\dot{h}$. Indeed, the negative disk velocity between $t = 0.004$ s and $t = 0.008$ s, which is higher in the dynamic case than in the quasi-steady case, coincides with a flow force, which is higher in the dynamic than in the quasi-steady simulation.

Conclusions

A CFD tool has been developed for accurate prediction of the discharge coefficient and flow force exerted on the valve disk, which is also applicable at special operating conditions outside the standard domain. For example, the spring tables can be adjusted, special closing pressures can be determined, or the tool can be used for design optimization purposes when a valve test has not been conducted yet. Its strength is to optimize valve geometries by means of sensitivity studies to account for geometric changes and physical properties, like cavitation or real-gas effects. The model also allows to adjust proper opening characteristics and to improve the opening stability of the valve. In this way, the number of necessary additional experiments can be significantly reduced.

A high-pressure test facility has been designed and constructed to conduct valve tests at well-defined measurement conditions to measure the valve characteristics and to provide data for validation of the CFD tool. In the test facility, the maximum liquid mass flow rate is 40 kg/s during 40 s for water and 10 kg/s for gaseous nitrogen.

For high-pressure liquid flows, an extension of the valve model to account for cavitation effects has resulted in significantly reduced deviations between the results of the numerical model and experiment, especially for the disk force. Although this cavitation model provides essential insight into local pressure and liquid volume fraction distributions, it needs to be further improved with respect to heat transfer and compressibility effects of the vapor phase to completely account for the observed deviations between experimental and numerical results.

For high-pressure single-phase gas flows excellent agreement between experiment and numerical results has been observed for the discharge capacity. However, a constant deviation between the experimentally and numerically determined disk force has been found. A dynamic analysis of an opening valve has led to force curves consistent to the experimental results. Furthermore, this dynamic multimesh model allows to model the opening characteristic of a safety valve. Moreover, it has provided insight into the cause of the force deviations between the experimental and numerical simulation results.

The experiments and the numerical calculations on a commercial high-pressure proportional safety valve have shown that for liquid as well as gas flows the discharge coefficient of this valve type is independent of the valve set pressure up to 600 bar. The conclusion is that the constant discharge coefficient is consistent with manufacturers' data and the conventional valve sizing method as long as accurate property data accounting for real-gas effects by means of an equation of state are used.

Literature Cited

1. ISO. Safety devices for protection against excessive pressure. I. Safety valves, EN ISO 4126-1:2004. Berlin: Beuth Verlag GmbH, 2004.
2. Zahariev T. Berechnung der Durchströmung und der Kennwerte von Sicherheitsventilen, PhD thesis. Magdeburg, Germany: Otto-von Quericke-Universitt Magdeburg, 2001.
3. Bredau J. Numerische Strömungsberechnung und experimentelle Strömungsvisualisierung in der Pneumatik, PhD thesis. Dresden, Germany: TU Dresden, 2000.
4. Bürk E. Numerische Strömungsberechnung ergänzt durch experimentelle Methoden zur Untersuchung pneumatischer Strömungen, PhD thesis. Dresden, Germany: TU Dresden, 2006.
5. Darby R, Molavi K. Viscosity correction factor for emergency relief valves. *Process Saf Prog*. 1997;16:80–82.
6. Föllmer B, Schnettler A. Challenges in designing API safety relief valves. *Valve World*. 2003;10:39–43.
7. Moncalvo D, Friedel L, Jörgensen B, Höhne T. Sizing of safety valves using ANSYS CFX-Flo®. *Chem Eng Technol*. 2009;32:247–251.
8. Beune A. Analysis of high-pressure safety valves, PhD thesis. Eindhoven, The Netherlands: Eindhoven University of Technology, 2009.
9. Schmidt J, Peschel W, Beune A. Experimental and theoretical studies on high pressure safety valves: Sizing and design supported by numerical calculations (CFD). *Chem Eng Technol*. 2009;32:252–262.

10. Rist D. *Dynamik Realer Gase*. Berlin: Springer-Verlag, 1996.
11. ANSYS. *Manual ANSYS CFX, Release 11.0*. Canonsburg: ANSYS, 2006.
12. Menter FR. Two-equation eddy-viscosity turbulence models for engineering applications. *AIAA J*. 1994;32:1598–1605.
13. Soave G. Equilibrium constants from a modified Redklich-Kwong equation of state. *Chem Eng Sci*. 1972;27:1197–1203.
14. IUPAC. International Union of Pure and Applied Chemistry: IUPAC Chemical Data Series, 2008. Available at: http://www.iupac.org/
15. Rhie CM, Chow WL. Numerical study of the turbulent flow past an airfoil with trailing edge separation. *AIAA J*. 1983;21:1525–1532.
16. Koenig H, Friedel L. Messung des transienten Massenaustrages und der kurzzeitigen thermofluiddynamischen Vorgänge während der Reaktorentlastung. *Forsch Ingenieurwes*. 2005;70:215–219.
17. ISO. Measurement of fluid flow by means of pressure differential devices inserted in circular cross-section conduits running full, EN ISO 5167: 2003. Berlin: Beuth Verlag GmbH, 2003.
18. Beinert C. Eignung numerischer Strömungssimulation zur Bestimmung des Betriebsverhaltens von Industriearmaturen, PhD thesis. Darmstadt, Germany: TU Darmstadt, 2007.
19. Singhal AK, Athavale MM, Li H, Jiang Y. Mathematical basis and validation of the full cavitation model. *J Fluid Eng-Trans ASME*. 2002;124:617–624.
20. NIST. NIST Chemistry WebBook, NIST Standard Reference Database Number 69, 2009. Available at: http://webbook.nist.gov/chemistry/
21. Reid RC, Sherwood TK. *The Properties of Gases and Liquids*, 2nd ed. New York: McGraw-Hill, 1966.
22. Roberts RA, Cui J. Numerical analysis of a pulsation damper fuel injection rails. *Int J Vehicle Syst Model Test*. 2006;1:312–328.

Appendix

In this appendix, it will be shown how the required thermodynamic properties for the look-up tables have been calculated in a thermodynamically consistent way from the EoS and experimental data on the specific heat. The compressibility factor Z equals

$$Z = \frac{p v}{R_s T} \qquad (A1)$$

with v the specific volume per unit of mass equal to $1/\rho$. The SRK EoS is given by

$$Z = \frac{v}{v - b} - \frac{a\alpha}{R_s T (v + b)} \qquad (A2)$$

where the coefficients a and b depend on the specific gas constant R_s, critical pressure p_c, and critical temperature T_c

$$a = 0.42747 \frac{R_s^2 T_c^2}{p_c} \qquad (A3)$$

$$b = 008664 \frac{R_s T_c}{p_c} \qquad (A4)$$

Furthermore, α is given by

$$\alpha = [1 + (0.480 + 1.574\omega - 0.176\omega^2)(1 - T_r^{0.5})]^2 \qquad (A5)$$

where the acentric factor ω depends on the reduced pressure $p_r = p/p_c$ and the reduced temperature $T_r = T/T_c$

$$\omega = -1 - \log_{10}(p_r)_{T_r=0.7} \qquad (A6)$$

To calculate the thermodynamic properties as a function of p and T it is chosen to combine the EoS (A2) with the specific

heat capacity at constant pressure c_p as a function of temperature at one value of the pressure p_{ref}. This is the minimal set of information wherefrom all thermodynamic states in the whole pressure and temperature domain can be derived in a thermodynamically consistent way, i.e., by obeying the Maxwell relations. This is important for numerical stability of the solution process. It is convenient to choose p_{ref} as low as possible, so that the fluid behaves as an ideal gas and remains in the gas phase for all values of T at this pressure.

The first law of thermodynamics for the specific enthalpy difference dh reads

$$dh = c_p dT + \left[v - T \left(\frac{\partial v}{\partial T} \right)_p \right] dp \qquad (A7)$$

which becomes in combination with the general real-gas EoS

$$dh = c_p dT - K_T v dp \qquad (A8)$$

Here, K_T denotes the temperature derivative of the compressibility factor:

$$K_T = \left(\frac{T}{Z} \frac{\partial Z}{\partial T} \right)_p \qquad (A9)$$

which is zero for perfect gases as $Z = 1$. The specific enthalpy can now be calculated at any combination of p and T from (20):

$$h(p, T) = h_{ref} + \int_{T_{ref}}^{T} c_p(p_{ref}, \tilde{T}) d\tilde{T} - \int_{p_{ref}}^{p} K_T(\tilde{p}, T) v(\tilde{p}, T) d\tilde{p} \qquad (A10)$$

where $h_{ref} = h(p_{ref}, T_{ref})$ is a reference value. The reference temperature T_{ref} is chosen as high as possible to avoid erroneous computations initiated by discontinuities around the thermodynamic critical point while filling the table. For the construction of the look-up tables, (A10) has been discretized with the trapezoidal rule and sufficiently small pressure and temperature intervals. The same procedure accounts for the specific entropy s

$$ds = c_p \frac{dT}{T} - \left(\frac{\partial v}{\partial T} \right)_p dp \qquad (A11)$$

The specific entropy can then be integrated with the trapezoidal rule as well

$$s(p, T) = s(p_{ref}, T_{ref}) + \int_{T_{ref}}^{T} c_p(p_{ref}, \tilde{T}) \frac{d\tilde{T}}{\tilde{T}}$$
$$- \int_{p_{ref}}^{p} \left(\frac{\partial v}{\partial T} (\tilde{p}, T) \right)_{\tilde{p}} d\tilde{p} \qquad (A12)$$

The specific heat c_p can be derived in a similar way by using the Maxwell relation

$$\frac{\partial c_p}{\partial p} = \frac{\partial}{\partial T} \left(v - T \left(\frac{\partial v}{\partial T} \right)_p \right) \qquad (A13)$$

This leads to

$$c_p(p,T) = c_p(p_{ref},T) + \int_{p_{ref}}^{p} \frac{\partial}{\partial T}\left(v - T\left(\frac{\partial v}{\partial T}\right)_p\right)_{\tilde{p}} d\tilde{p} \quad (A14)$$

In the valve sizing method (5), the adiabatic exponent κ (6) has to be substituted with a real-gas formulation when deviations from the perfect gas approximation become significant. The adiabatic exponent is defined as the ratio of isentropic pressure-density fluctuations

$$\kappa \equiv -\frac{v}{p}\left(\frac{\partial p}{\partial v}\right)_s \quad (A15)$$

For real gases, the adiabatic exponent is given by[10]

$$\kappa = \frac{c_p}{c_p[1 - K_p] - ZR_s[1 + K_T]^2} \quad (A16)$$

where K_p is the pressure derivative of the compressibility factor Z

$$K_p = \left(\frac{p}{Z}\frac{\partial Z}{\partial p}\right)_T \quad (A17)$$

For the test fluid nitrogen, the specific heat capacity at constant pressure per unit mass is taken from tabulated values generated in the fluid property database NIST[20] with 0.3–0.8% uncertainty at low temperatures up to 2000 K and at a constant reference pressure of 0.01 bar. For higher temperatures up to 6000 K, a polynomial fit from the same database is used.

The accuracy of the calculated compressibility factor Z and specific heat capacity at constant pressure c_p has been compared with IUPAC[14] reference data for nitrogen. For reduced temperatures $T_r > 1.5$ the accuracy of both variables is within 5% at pressures up to 3600 bar.

For the CFD code, it is essential that all quantities are thermodynamically consistent with each other so that a unique solution can exist at each integration point. The IUPAC tables deliver more accurate data, but these are supplied only for pure gases and do not cover the pressure and temperature region necessary for the CFD code. Linear interpolation close to the critical point and extrapolation to low and high temperatures could lead to inconsistencies and failure of the CFD solver. A much wider application range to calculate the specific volume of the gas can be covered if no experimental data are available by means of an EoS. Therefore, the cubic SRK EoS is chosen.

The dynamic viscosity $\mu(p,T)$ is defined according to the rigid, noninteracting sphere model.[21] Furthermore, the thermal conductivity $\lambda(p,T)$ is defined according to the modified Euken model.[21]

To prevent CFX solving outside the single-phase region during the iterative solution process, the saturated vapor pressure curve according to Gomez-Thodos[21] is used. At pressures higher than the critical pressure and close to the critical temperature, the EoS leads to increased inaccuracies. For this reason, the saturated vapor pressure curve is shifted to an artificial critical temperature 1.05 T_r. Above this temperature, all thermodynamic quantities are continuous functions of pressure and temperature.

For liquid flows at high pressures, the density is no longer constant but varies with pressure[22]

$$\frac{1}{v} = \frac{1}{v_{amb}}\left(\frac{p - p_{amb}}{K} + 1\right) \quad (A18)$$

where the pressure p_{amb} and specific volume v_{amb} are at standard temperature and pressure, and K is the bulk modulus.